ADVANCED ELECTRONIC MATERIALS Open Access
www.advelectronicmat.de

Strained Organic Thin-Film Single Crystals for High-Mobility and High-Frequency Transistors

Mizuki Abe, Yu Yamashita, Taiki Sawada, Tatsuyuki Makita, Shohei Kumagai, Shun Watanabe, and Jun Takeya**

Transistors fabricated from thin-film single crystals of organic semiconductors (OSCs) have exhibited high mobility exceeding 10 $cm^2 V^{-1} s^{-1}$ and show compatibility with low-cost solution processing. However, their carrier mobility is limited by the molecular vibrations in their soft lattices. This study establishes a practical method for applying compressive strain to single-crystal OSCs to enhance mobility and transistor performance. In this method, a polymer film substrate is bent to mechanically stretch its surface. Organic single-crystal transistors are then laminated onto the stretched surface of substrate. Releazing the stretch by recovering the flat surface of the substrate allowed the transistors to be compressed by up to 3%. This resulted in a 52% increase in mobility, reaching 26.4 $cm^2 V^{-1} s^{-1}$. X-ray diffraction measurements confirmed lattice strain in the OSC single crystals. Moreover, carrier mobility and cutoff frequency increased in MHz-operating short-channel transistors, demonstrating applicability for high-frequency devices. The mobility increase is maintained even three years after introducing the 1% compressive strain, possibly owing to the flexible, molecularly thin characteristics of OSC single crystals. The proposed strain management methods may provide new avenues to enhance the performance of high-mobility and high-frequency electronic devices based on OSC thin-film single crystals.

1. Introduction

Single-crystal thin films of organic semiconductors (OSCs)[1–8] exhibit flexibility, stability, and high mobility, positioning them as suitable candidates for electronic devices fabricated via low-cost solution processes. Organic thin-film transistors (OTFTs) made from OSC single crystals find applications in devices such as wireless communication tags,[9,10] complementary circuits,[11] and sensors.[5,12,13] The cutoff frequency of OTFTs can exceed the very high-frequency band (≈30 MHz) owing to high mobility values around 10 $cm^2 V^{-1} s^{-1}$ in band-transporting materials.[14–17] Although enhancing mobility would facilitate high-frequency device development, carrier scattering from molecular vibrations restricts OSC mobility at room temperature.[18–20] Researchers have relied on advanced molecular designs, including design, synthesis, and evaluation of new molecules, to reduce the effects of molecular vibrations[21,22] and in advancing organic electronics.

Strain serves as an external factor that can improve carrier mobility and operational frequency in semiconductor devices. In inorganic semiconductors, the modulation of the crystal structure by external strain can modify the effective mass and carrier mobility,[23] known as the piezoelectric effect.[24] A representative example is the strained silicon metal oxide field-effect transistor,[25–27] where persistent strain is applied around the interface of epitaxially grown materials with different lattice constants to enhance mobility and operating frequency.

Strain engineering in flexible electronics[28–31] could be crucial for improving the device properties of OSC single crystals. Studies have demonstrated enhancements in carrier mobility by applying strains that uniformly modify lattice constants.[13,30,32–37] For example, a 2.9% uniaxial strain can increase mobility by up to 70%, largely due to the reduced molecular vibration amplitude and increased carrier relaxation time.[36] Such uniaxial strain is achieved by bending the substrates, leveraging the flexibility and small Young's modulus of OSCs compared to those of inorganic materials.[38,39] However, this approach requires the substrate to remain bent with a very small curvature radius, typically less than 1 cm, to induce strain of up to 3%, which is

M. Abe, Y. Yamashita, T. Sawada, T. Makita, S. Watanabe, J. Takeya
Department of Advanced Materials Science
Graduate School of Frontier Sciences
The University of Tokyo
5-1-5 Kashiwanoha, Kashiwa, Chiba 277-8561, Japan
E-mail: YAMASHITA.Yu@nims.go.jp; takeya@k.u-tokyo.ac.jp
Y. Yamashita, J. Takeya
Research Center for Materials Nanoarchitectonics (MANA)
National Institute for Materials Science (NIMS)
1-1 Namiki, Tsukuba, Ibaraki305-0044, Japan
S. Kumagai
Department of Chemical Science and Engineering
School of Materials and Chemical Technology
Institute of Science Tokyo
4259-G1-7 Nagatsuta, Midori-ku, Yokohama, Kanagawa 226-8501, Japan
The ORCID identification number(s) for the author(s) of this article can be found under https://doi.org/10.1002/aelm.202500144

DOI: 10.1002/aelm.202500144

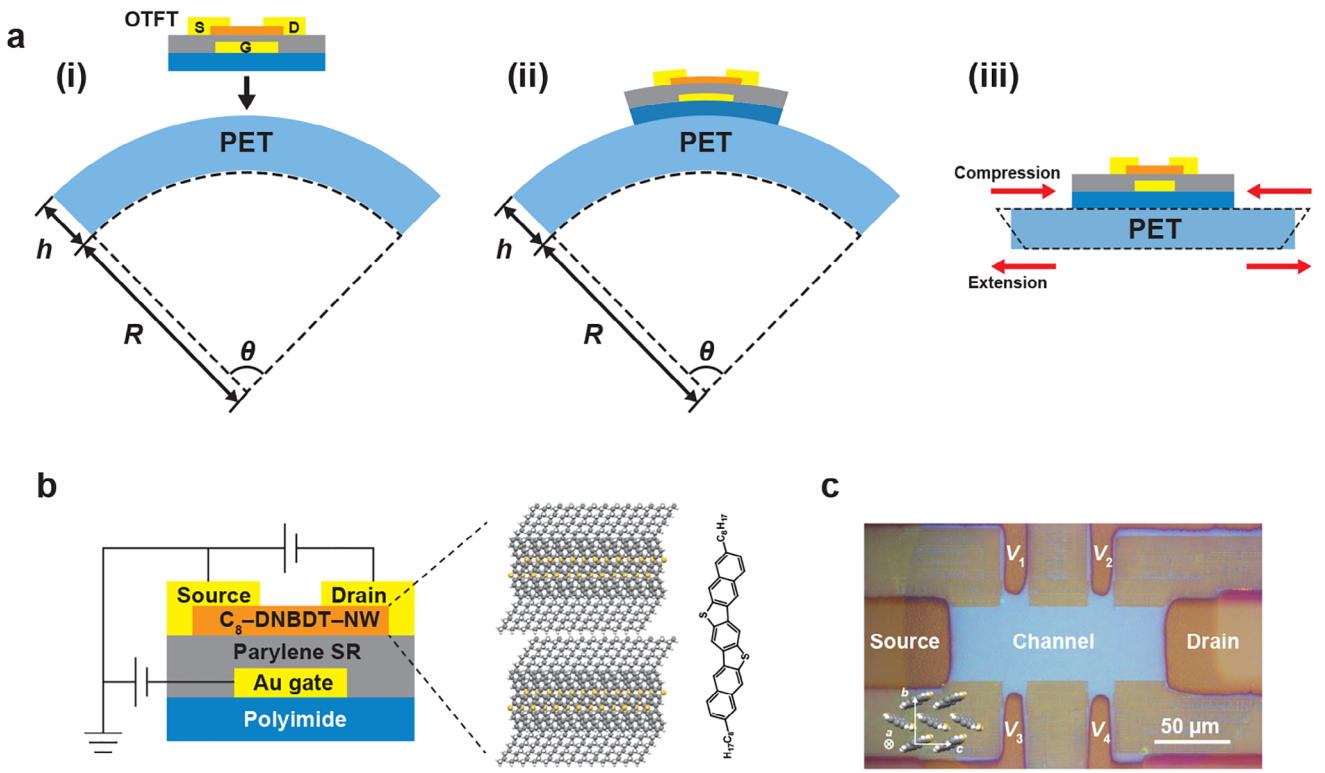

Figure 1. Method to induce persistent strain in organic thin-film transistors (OTFTs). a) Schematic of the method to induce persistent strain in OTFTs. b) Schematic of the device structure and packing and chemical structures of C_8–DNBDT–NW. c) Polarized optical microscope image of the fabricated transistor. The channel direction is parallel to the *c*-axis of the single crystal.

unsuitable for practical applications. Alternatively, lattice strain can be induced in OSCs by varying the solution shearing speed during crystal growth.[32,40] However, this method yields lower strain magnitudes compared to the bending method, resulting in considerable expansion in one crystal axis when shrinkage occurs in another. Additionally, strain relaxation at the OSC/substrate interface occurs through weak van der Waals forces. Thus, a novel method for inducing strain in OSC single crystals could enhance mobility and performance in OTFTs.

This study developed a practical method to induce uniaxial compressive lattice strain in OSC thin-film single crystals, enhancing mobility and cutoff frequency. Single-crystal OTFTs fabricated on flexible thin substrates were attached to the convex surface of a bent mother substrate (**Figure 1**a(i), (ii)). Upon releazing the bending, the OTFTs experienced strain according to the change in the mother substrate's surface length (Figure 1a(iii)). This method produced uniform strain in the OSC single crystal, as confirmed via X-ray diffraction (XRD) measurements. Uniaxial lattice strain was controlled by modifying the initial curvature of the mother substrate. We applied strain levels of up to 3%, resulting in a mobility increase of 50%, reaching 26.4 $cm^2 V^{-1} s^{-1}$. Additionally, the cutoff frequency of the OTFT with a 10 μm channel length increased by 40% with persistent 1% compressive strain. Our findings highlight the effectiveness of strain engineering in organic, flexible electronics, providing opportunities for enhancing mobility and device performance.

2. Results and Discussion

We fabricated transistors with a bottom-gate top-contact structure to investigate the effect of lattice strain on the performance of single-crystal OTFTs. We used thin-film single crystals of 3,11-dioctyldinaphtho[2,3-*d*:2',3'-*d'*]benzo[1,2-*b*:4,5-*b'*]dithiophene(C_8–DNBDT–NW)[14] as the active layer on a 16 μm-thick polyimide (PI) substrate (Figure 1b). The gate electrode and gate dielectric were thermally deposited with Au (40 nm) and Parylene-SR (200 nm), respectively. A-few-molecular-layer thick single crystals of C_8–DNBDT–NW were deposited on the Parylene-SR layer via the continuous edge-casting method,[2,8] a meniscus-guided coating method. The Au source and drain contacts were thermally deposited through a shadow mask with a channel length of 240 μm and a width of 80 μm. The crystal growth direction of C_8–DNBDT–NW is aligned parallel to the channel of the OTFTs, ensuring that the charge transport direction aligned with the crystal's *c*-axis (Figure 1c).

We developed a novel method to induce persistent compressive strain in OTFTs. OTFTs prefabricated on a PI substrate were tightly attached to a convexly bent polyethylene terephthalate (PET) mother substrate (Figure 1a(i), (ii)) using a cyanoacrylate adhesive (CC-33A, KYOWA). The thickness of the PET mother substrate is 500 μm, more than 30 times that of the PI substrate of our OTFTs. When the PET mother substrate is convexly bent, its upper surface is stretched, whereas the lower surface is compressed. The OTFTs attached to the stretched surface of

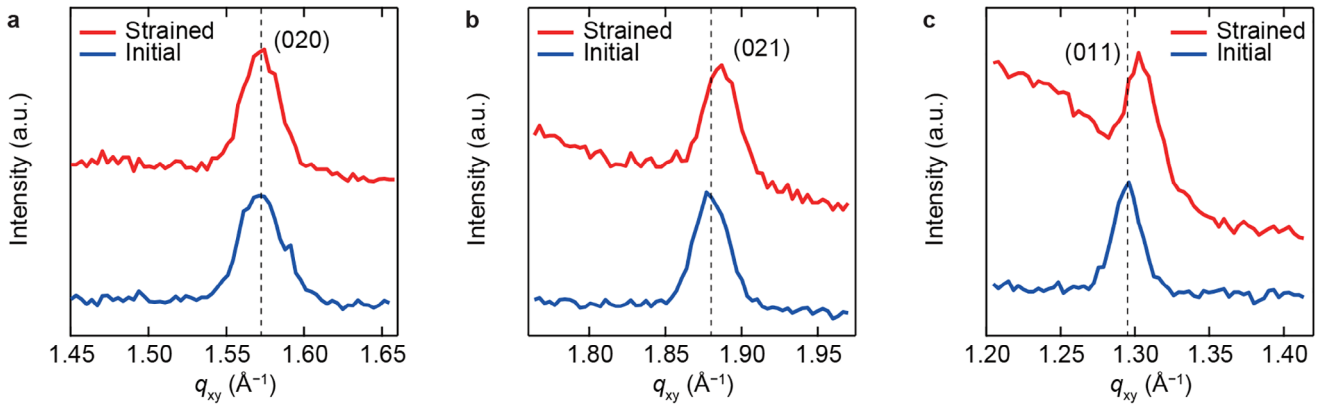

Figure 2. Bragg peak shifts of the organic semiconductor (OSC) single crystal by mechanical strain. Results of X-ray diffraction measurements of (a) (020), (b) (021), and (c) (011) surfaces of C_8–DNBDT–NW single crystals. Blue lines show the results for the initial state and red lines show those after inducing a nominal strain of −0.98%.

the mother substrate endured persistent compression when the mother substrate returned to a flat state. The surface strain ε of a bent film is expressed as follows:[41]

$$|\varepsilon| \approx \frac{h_s}{2R} \tag{1}$$

where R is the radius of curvature, and h_s is the film thickness. A positive ε represents tensile strain, while a negative value indicates compressive strain. When the thickness of the OTFT is considerably smaller than that of the mother substrate, the strain applied to the OTFT as the mother substrate returns to the flat state can be approximated as follows:

$$|\varepsilon| = \frac{h_{ms}}{2\left(R + \frac{h_{OTFT}}{2} + h_{ms}\right)} \approx \frac{h_{ms}}{2\left(R + h_{ms}\right)} \tag{2}$$

where h_{OTFT} and h_{ms} are the thicknesses of the OTFT and mother substrate, respectively. Thus, the strain applied to our OTFTs can be controlled by adjusting the thickness and curvature of the mother substrate. To secure the OTFTs to the PET mother substrate, we attached the PET mother substrate to a cylindrical surface to allow precise control over the curvature radius (Figure S1, Supporting Information). The *c*-axis of C_8–DNBDT–NW aligned with the circumferential direction of the cylinder, where compressive strain was applied. In the following experiments, we maintained a constant h_{ms} of 500 µm and varied the R values.

We determined changes in the lattice constants of C_8–DNBDT–NW single crystals using XRD measurements conducted before and after attaching the OTFT substrates to the mother substrates. Due to the substantial thickness of the mother substrate, minimizing background noise was crucial to observing the diffraction peaks of the single crystals. Instead of the transmission setups commonly employed for single crystals, we used the grazing-incidence X-ray diffraction (GIXD) method owing to its high surface sensitivity. **Figure 2** shows the Bragg diffraction peaks from the C_8–DNBDT–NW single crystal, while **Table 1** lists the changes in lattice constants before and after attaching the OTFT substrate to the mother substrate. The detailed fitting procedures are shown in Figures S2 and S3 (Supporting Information). In this measurement, the curvature of the mother substrate was controlled to apply a strain of −0.98% to the OTFT substrate. The lattice constant along the *c*-axis was decreased by 1.1% based on the observed shifts in the (021) and (011) diffraction peaks. This correlation between the predicted and observed strains suggests that our method effectively induces controlled lattice strain in the OSC thin-film single. The width of the diffraction peaks did not increase upon application of strain, supporting the uniformity of the lattice constant in the fabricated sample (Table S1, Supporting Information). In addition, the lattice constant along the *b*-axis increased by only 0.03%, confirming that uniaxial strain mainly occurred along the *c*-axis with our method.

We confirmed enhanced mobility by our method through four-terminal measurements of single-crystal OTFTs. The measurements were conducted on OTFTs with a long channel length (L = 240 µm), eliminating the influence of contact resistance. Unstrained OTFTs exhibit nearly ideal transfer and output characteristics (**Figure 3a–c**), achieving four-terminal mobility of 17.4 $cm^2 V^{-1} s^{-1}$ (Figure 3d). This OTFT was attached to the mother substrate such that a compressive strain could be

Table 1. Changes in lattice constants of C_8–DNBDT–NW when applying a nominal strain of −0.98%. The lattice constant errors are calculated from the standard deviation of the peak positions of each crystal surface from measurements taken at various incident angles ϕ. See Figure S2 (Supporting Information) for details.

	Lattice constant		Strain	
	b [Å]	*c* [Å]	ε_b [%]	ε_c [%]
Initial	7.991 ± 0.004	6.10 ± 0.01	—	—
Strained	7.994 ± 0.004	6.03 ± 0.01	+0.03 ± 0.06	−1.1 ± 0.3

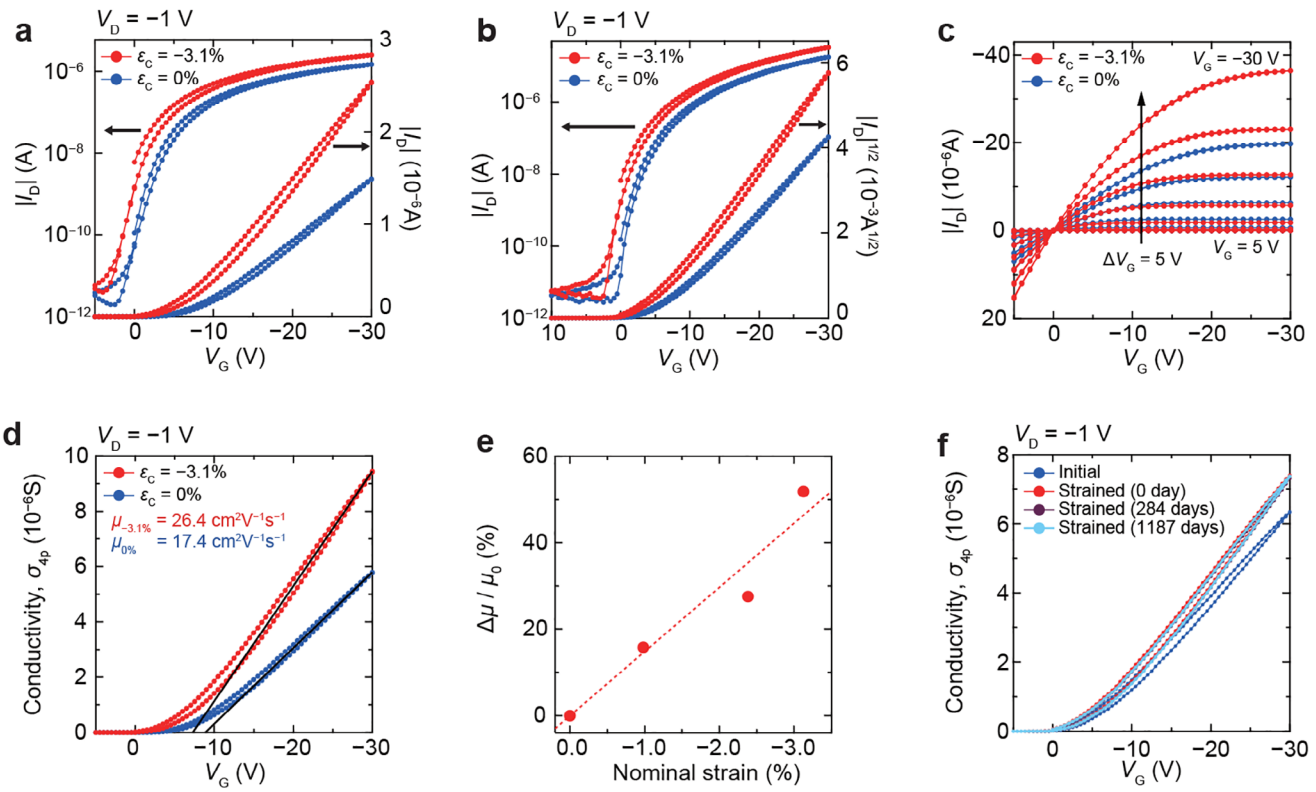

Figure 3. Enhancement of static performances of OTFTs by applying persistent strain. Transfer properties in a) linear and b) saturation regions; c) Output properties. d) Gate voltage dependence of the four-terminal conductivity. The career mobilities extracted from these plots are also shown. e) Dependence of the changes in four-terminal mobility on the nominal strain. f) Gate voltage dependence of the four-terminal conductivity of our OTFT in the initial state (blue), after inducing −0.98% strain (red), and 284 days after inducing the strain (purple), and 1187 days after inducing the strain (light blue).

applied along the *c*-axis of C_8–DNBDT–NW, which is the channel direction of our OTFTs. The curvature radius of the mother substrate was controlled (R = 7.5mm) to introduce a nominal strain of −3.1%. After applying the strain, the four-terminal mobility increased by 52%, reaching 26.4 $cm^2 V^{-1} s^{-1}$. Smaller strain performances are shown in Figures S4 and S5 (Supporting Information), where all devices exhibited increased mobility following compressive strain without significant degradation in transport properties. Notably, the four-terminal mobility increased monotonically with the applied nominal compressive strain (Figure 3e), which is consistent with our previous findings.[36] This demonstrates that a compressive strain of up to 3% enhances mobility. We attribute the mobility enhancement to the suppression of molecular vibration rather than changes in effective mass;[36,42] a reduction in the lattice constant of C_8–DNBDT–NW directly restricts the molecular vibrations associated with electron–phonon coupling.

We verified the persistence of the compressive strain in our OTFTs by measuring the changes in four-terminal mobility over time. After inducing strain, OTFT was restored in a vacuum desiccator to mitigate environmental influences. Notably, the mobility of the OTFT strained by −1% remained stable even after 1187 days (Figure 3f). OTFTs with larger strain also showed moderate stability of performances (Figure S6, Supporting Information). These findings verify suppressed strain relaxation at the interface between the OSC thin-film single crystals and substrate. The OSC film thickness is only 10 nm, and Young's modulus for OSCs is typically more than one order of magnitude lower than that of inorganic materials.[39] Therefore, the stress at the semiconductor/substrate interface appears sufficiently low to suppress strain relaxation.

In OTFT applications, improving mobility and cutoff frequency (f_T) is crucial for enhancing dynamic performance. The cutoff frequency, defined as the maximum frequency at which a transistor can amplify a signal, is given by

$$f_T = \frac{g_m}{2\pi C_G} \tag{3}$$

where g_m is the transconductance ($= \frac{\partial I_D}{\partial V_G}$) and C_G is the total capacitance, including gate and parasitic capacitances. In top-contact bottom-gate OTFTs, parasitic capacitance primarily results from the overlap between the gate and source/drain electrodes, referred to as the contact length (L_C). Therefore, a large carrier mobility, short channel length (L), and short contact length are necessary for enhancing cutoff frequency. To evaluate the effect of lattice strain on the dynamic properties of OTFTs, a short-channel transistor was fabricated on a 16 μm-thick PI substrate using photolithography to pattern the electrodes. The channel and contact lengths of this device were 10 and 5 μm,

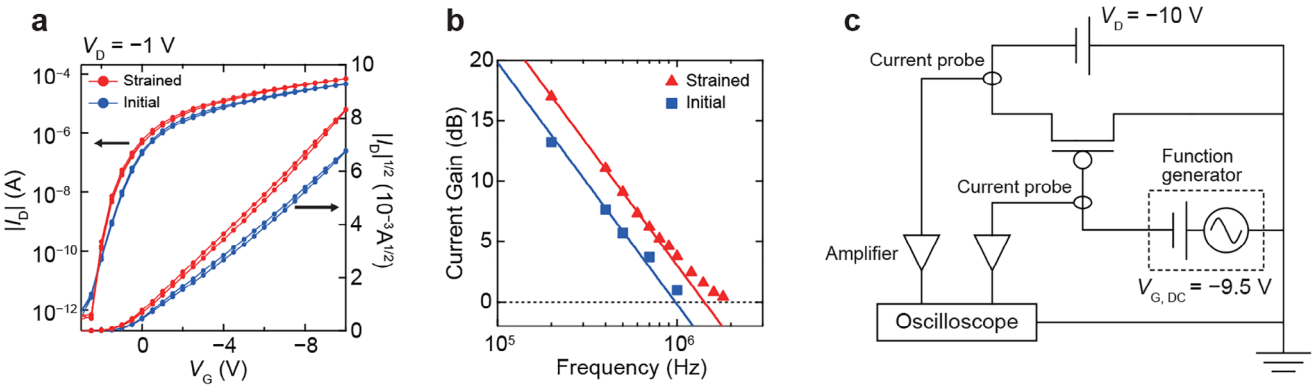

Figure 4. Enhancement of static and dynamic performances of a short channel OTFT. a) Static transfer properties before and after strain. b) Frequency dependence of the current gain before and after strain. c) Schematic of the cutoff frequency measurement setup.

respectively. Static and dynamic characteristics were evaluated before and after applying a compressive strain (**Figure** 4a,b) of −0.98% along the *c*-axis. Before inducing strain, the short-channel OTFT demonstrated an effective mobility of 0.71 $cm^2 V^{-1} s^{-1}$ in the saturation regime. After inducing strain, the effective mobility increased to 1.01 $cm^2 V^{-1} s^{-1}$, marking a 40% improvement. Owing to the effect of contact resistance, the mobility of the short-channel device is smaller than the intrinsic value obtained from four-terminal measurements. Note that the contact resistance can be decreased by strain application, which is supported in our long-channel four-terminal measurements (Figure S7, Supporting Information). This can be attributed to an increase in carrier mobility within the overlap region between the contact and gate electrodes.[43] The cutoff frequency was experimentally measured by observing the frequency at which the transistor's current gain dropped to 0 dB using the setup shown in Figure 4c. The current gain, defined as the ratio of the drain current amplitude (ΔI_G) to the gate current amplitude (ΔI_D), decreased as a function of f^{-1}. The measured f_T was 0.98 MHz before strain application. After inducing strain, the current gain in the dynamic measurements increased, and the extracted cutoff frequency increased to 1.4 MHz, showing a 40% improvement. The cutoff frequency in the saturation region can be expressed as follows:[14,44–47]

$$f_T = \frac{\mu_{eff}|V_G - V_{Th}|}{2\pi L\left(\frac{2}{3}L + 2L_C\right)} \quad (4)$$

where μ_{eff} is the effective mobility of the transistor and V_{Th} is the threshold voltage. The increase in the cutoff frequency can be ascribed to the increase in effective mobility in our case. Our findings demonstrate that introducing persistent lattice strain effectively improves the static and dynamic responses of single-crystal OTFTs.

Our findings highlight the importance of strain engineering in flexible electronics using thin-film single crystals. For OSC thin-film single crystals, the lattice strain was preserved on flexible substrates even without covalent bonding between the crystals and substrates. Our method may allow for the controlled application of strain to various thin-film single crystals and devices, not limited to those of OSCs, with potential increases in achievable strain through substrate material design. In addition, in flexible electronics, substrates undergo shrinkage and expansion during solution processing and heating, altering the lattice constants of overlying single crystals. Thus, the lattice constants and physical properties of thin-film single crystals may differ from those of bulk materials owing to the residual strain. The GIXD measurements employed in this study can evaluate strain in these thin films under the same device-operating conditions.

3. Conclusion

This study developed a practical method to induce lattice strain in OSC thin-film single crystals. Uniaxial lattice strain in OSC single crystals was confirmed by GIXD measurements. The four-terminal mobility of strained OTFT increased by 52%, reaching 26.4 $cm^2 V^{-1} s^{-1}$ with a nominal compressive strain of 3.1% in the flattened state. This highlights the advantages over the conventional bending method, which requires the device to remain bent with a very large curvature. The induced strain of −0.98% remained almost stable even after three years, demonstrating the feasibility of maintaining lattice strains in molecularly thin OSC single crystals on flexible substrates. The mobility enhancement also raised the cutoff frequency of our MHz-operating OTFT. Further advancements in interface engineering may yield larger and more stable lattice strains. The strain engineering demonstrated here provides opportunities to control and enhance the performance of high-mobility, high-frequency electronic devices using OSC thin-film single crystals.

4. Experimental Section

Device Fabrication: All devices in this study were fabricated on a 16 µm-thick PI film (zenomax®). The PI film was pre-laminated onto glass and peeled off after fabricating the OTFT devices. Gold was thermally evaporated to form the gate electrode. Parylene-SR (KISCO Ltd.) was deposited via chemical vapor deposition, achieving a gate dielectric thickness of 200 nm. Single-crystal film of C_8–DNBDT–NW was grown on the Parylene-SR layer via a continuous edge-casting method from a 0.010wt.% 3-chlorothiophene solution at 63°C. A 40 nm thick gold layer was thermally deposited through the shadow mask to form the source-drain contact electrodes and voltage probe on the C_8–DNBDT–NW layer. Dry

etching of the OSC layer was performed using a Yttrium Aluminum Garnet Laser (V-Technology Co., Ltd., Callisto (266 nm)).

OTFT devices for high-frequency measurements were fabricated via photolithography to pattern the gate, source, and drain electrodes. Cr (1.5 nm)/Au (20 nm)/Cr (1.5 nm) layer was patterned via a lift-off process to define the gate electrode. TLOR (Tokyo Ohka Kogyo Co., Ltd.), NMD-3 (Tokyo Ohka Kogyo Co., Ltd.), and 1-Methyl-2-Pyrrolidone were used as the positive photoresist, developer, and remover, respectively. As a gate dielectric, a 60 nm thick aluminum oxide was deposited via atomic layer deposition, followed by Parylene-SR (50 nm) via chemical vapor deposition. A single crystal 3,11-dinonyldinaphtho[2,3-*d*:2',3'-*d*']benzo[1,2-*b*:4,5-*b*']dithiophene (C_9–DNBDT–NW) was transfered[48] onto the Parylene-SR layer to serve as the active layer. The gold contact electrodes were patterned using multiple photographic processes, utilizing AZ5214E (Merck) and AURUM S-50790 (Kanto Chemical Co., Ltd.) as the positive photoresist and gold etchant, respectively. All lithographic processes were performed using a maskless aligner (MLA150, Heidelberg Instruments).

X-ray Diffraction Measurement: For X-ray diffraction measurements, C_8–DNBDT–NW was deposited on a PI substrate covered by Parylene-SR via continuous edge-casting, achieving a mono-domain single crystal after wet-etching with 1,2,3,4-tetrahydronaphtalene. GIXD measurements were conducted using SmartLab-2D/ME/T (Rigaku) with CuK_α radiation (λ = 0.154187 nm at room temperature) to quantify changes in the C_8–DNBDT–NW lattice constant.

Electrical Measurement: All electrical measurements were conducted under dark and ambient conditions. The static transistor properties were measured using a semiconductor parameter analyzer (Keithley 4200-SCS). Four-terminal conductivity was calculated by following equation, $\sigma_{4T} = (L_{4T}/W)(|I_D/(V_1 - V_2)|)$, where L_{4T} was length between a pair of voltage probes and V_1, V_2 were the potential indicated by voltage probe. Similarly, the four-terminal mobility was obtained from the following expression, $\mu_{int} = (1/C_i)(\partial\sigma_{4T}/\partial V_G)$, where C_i was the capacitance per unit area of gate dielectric. The high-frequency responses were measured using a digital phosphor oscilloscope (Tektoronix TDS3014C). AC voltage signals of 1 V peak-to-peak and a −9.5 V DC offset were generated using a function generator (Tektronix AFG3102) for the gate voltage, while a DC drain voltage of −10 V was applied using a semiconductor parameter analyzer. The output signals of the gate and drain voltages were measured using an oscilloscope equipped with current probes (Tektronix CT-6).

Supporting Information

Supporting Information is available from the Wiley Online Library or from the author.

Acknowledgements

This work was supported in part by JST CREST (JPMJCR21O3) and JSPS KAKENHI grants (JP22H04959).

Conflict of Interest

The authors declare no conflict of interest.

Author Contributions

M.A. and Y.Y. conceived of and designed the study. M. A. conducted the device fabrication and measurements. T.S. contributed to the high-frequency measurements. T. M. contributed to the fabrication of the short-channel device. Y.Y. and S.K. contributed to the GIXD analysis. S.W. and J.T. supervised the study.

Data Availability Statement

The data that support the findings of this study are available in the supplementary material of this article.

Keywords

flexible electronics, organic semiconductor, organic single crystal, strain, thin film transistor

Received: February 24, 2025
Revised: May 22, 2025
Published online: June 17, 2025

[1] Y. Diao, B. C. Tee, G. Giri, J. Xu, D. H. Kim, H. A. Becerril, R. M. Stoltenberg, T. H. Lee, G. Xue, S. C. Mannsfeld, Z. Bao, *Nat. Mater.* **2013**, *12*, 665.
[2] J. Soeda, T. Uemura, T. Okamoto, C. Mitsui, M. Yamagishi, J. Takeya, *Appl. Phys. Express* **2013**, *6*, 076503.
[3] C. Xu, P. He, J. Liu, A. Cui, H. Dong, Y. Zhen, W. Chen, W. Hu, *Angew. Chem. Int. Ed.* **2016**, *55*, 9519.
[4] H. T. Yi, M. M. Payne, J. E. Anthony, V. Podzorov, *Nat. Commun.* **2012**, *3*, 1259.
[5] B. Peng, S. Huang, Z. Zhou, P. K. L. Chan, *Adv. Funct. Mater.* **2017**, *27*, 1700999.
[6] I. Vladimirov, M. Kellermeier, T. Geßner, Z. Molla, S. Grigorian, U. Pietsch, L. Schaffroth, M. Kuhn, F. May, R. Weitz, *Nano Lett.* **2018**, *18*, 9.
[7] G. Kitahara, S. Inoue, T. Higashino, M. Ikawa, T. Hayashi, S. Matsuoka, S. Arai, T. Hasegawa, *Sci. Adv.* **2020**, *6*, eabc8847.
[8] S. Kumagai, T. Makita, S. Watanabe, J. Takeya, *Appl. Phys. Express* **2022**, *15*, 030101.
[9] E. Cantatore, T. C. Geuns, G. H. Gelinck, E. van Veenendaal, A. F. Gruijthuijsen, L. Schrijnemakers, S. Drews, D. M. De Leeuw, *IEEE J. Solid-State Circuits* **2006**, *42*, 84.
[10] A. Yamamura, H. Matsui, M. Uno, N. Isahaya, Y. Tanaka, M. Kudo, M. Ito, C. Mitsui, T. Okamoto, J. Takeya, *Adv. Electron. Mater.* **2017**, *3*, 1600456.
[11] X. Wei, S. Kumagai, T. Makita, K. Tsuzuku, A. Yamamura, M. Sasaki, S. Watanabe, J. Takeya, *Commun. Mater.* **2023**, *4*, 4.
[12] H. Wang, L. Deng, Q. Tang, Y. Tong, Y. Liu, *IEEE Electron Device Lett.* **2017**, *38*, 1598.
[13] S. Watanabe, R. Hakamatani, K. Yaegashi, Y. Yamashita, H. Nozawa, M. Sasaki, S. Kumagai, T. Okamoto, C. G. Tang, L.-L. Chua, P. K. H. Ho, J. Takeya, *Adv. Sci.* **2021**, *8*, 2002065.
[14] A. Yamamura, S. Watanabe, M. Uno, M. Mitani, C. Mitsui, J. Tsurumi, N. Isahaya, Y. Kanaoka, T. Okamoto, J. Takeya, *Sci. Adv.* **2018**, *4*, eaao5758.
[15] A. Yamamura, T. Sakon, K. Takahira, T. Wakimoto, M. Sasaki, T. Okamoto, S. Watanabe, J. Takeya, *Adv. Funct. Mater.* **2020**, *30*, 1909501.
[16] J. W. Borchert, U. Zschieschang, F. Letzkus, M. Giorgio, R. T. Weitz, M. Caironi, J. N. Burghartz, S. Ludwigs, H. Klauk, *Sci. Adv.* **2020**, *6*, eaaz5156.
[17] U. Zschieschang, U. Waizmann, J. Weis, J. W. Borchert, H. Klauk, *Sci. Adv.* **2022**, *8*, eabm9845.
[18] S. Illig, A. S. Eggeman, A. Troisi, L. Jiang, C. Warwick, M. Nikolka, G. Schweicher, S. G. Yeates, Y. Henri Geerts, J. E. Anthony, H. Sirringhaus, *Nat. Commun.* **2016**, *7*, 10736.
[19] S. Fratini, M. Nikolka, A. Salleo, G. Schweicher, H. Sirringhaus, *Nat. Mater.* **2020**, *19*, 491.
[20] H. Sato, S. A. Abd. Rahman, Y. Yamada, H. Ishii, H. Yoshida, *Nat. Mater.* **2022**, *21*, 910.
[21] K. Takimiya, I. Osaka, T. Mori, M. Nakano, *Acc. Chem. Res.* **2014**, *47*, 1493.
[22] T. Okamoto, C. P. Yu, C. Mitsui, M. Yamagishi, H. Ishii, J. Takeya, *J. Am. Chem. Soc.* **2020**, *142*, 9083.

[23] R. Roldán, A. Castellanos-Gomez, E. Cappelluti, F. Guinea, *J. Phys.: Condens. Matter* **2015**, *27*, 313201.
[24] C. S. Smith, *Phys. Rev.* **1954**, *94*, 42.
[25] S.-i. Takagi, J. L. Hoyt, J. J. Welser, J. F. Gibbons, *J. Appl. Phys.* **1996**, *80*, 1567.
[26] K. Rim, K. Chan, L. Shi, D. Boyd, J. Ott, N. Klymko, F. Cardone, L. Tai, S. Koester, M. Cobb, D. Canaperi, B. To, E. Duch, I. Babich, R. Carruthers, P. Saunders, G. Walker, Y. Zhang, M. Steen, M. Ieong, in *IEEE International Electron Devices Meeting 2003*. IEEE, Piscataway, NJ **2003**, pp. 3–1.
[27] S. E. Thompson, M. Armstrong, C. Auth, M. Alavi, M. Buehler, R. Chau, S. Cea, T. Ghani, G. Glass, T. Hoffman, C.-H. Jan, C. Kenyon, J. Klaus, K. Kuhn, Z. Ma, M. Brian, K. Mistry, A. Murthy, B. Obradovic, R. Nagisetty, P. Nguyen, S. Sivakumar, R. Shaheed, L. Shifren, B. Tufts, S. Tyagi, M. Bohr, Y. El-Mansy, *IEEE Trans. Electron Devices* **2004**, *51*, 1790.
[28] Y. Cho, J. Park, S. Jeong, H. Park, H. W. Kim, J. H. Oh, C. Yang, *Chem. Mater.* **2022**, *34*, 1554.
[29] Y. Cho, Z. Sun, G. Li, D. Zhang, S. Yang, T. J. Marks, C. Yang, A. Facchetti, *J. Am. Chem. Soc.* **2024**, *147*, 758.
[30] S. Lee, H. Yoo, S. Jeong, D. H. Kim, S.-H. Kang, Y. Choi, C. Yang, B. H. Lee, K. C. Lee, *Macromol. Rapid Commun.* **2025**, *46*, 2500018.
[31] J. Lee, S. Kang, E. Lee, J. Lee, T. W. Yoon, M.-J. Kim, Y. Cho, M. Xiao, Y. Boeije, W. Zhu, C. Yang, J.-W. Lee, S. Lee, G. Zhang, H. Sirringhaus, B. Kang, *EcoMat* **2025**, *7*, e12513.
[32] G. Giri, E. Verploegen, S. C. Mannsfeld, S. Atahan-Evrenk, D. H. Kim, S. Y. Lee, H. A. Becerril, A. Aspuru-Guzik, M. F. Toney, Z. Bao, *Nature* **2011**, *480*, 504.
[33] Y. Okada, K. Sakai, T. Uemura, Y. Nakazawa, J. Takeya, *Phys. Rev. B* **2011**, *84*, 245308.
[34] K.-i. Sakai, J. Takeya, *Electronics* **2014**, *3*, 255.
[35] M. A. Reyes-Martinez, A. J. Crosby, A. L. Briseno, *Nat. Commun.* **2015**, *6*, 6948.
[36] T. Kubo, R. Häusermann, J. Tsurumi, J. Soeda, Y. Okada, Y. Yamashita, N. Akamatsu, A. Shishido, C. Mitsui, T. Okamoto, S. Yanagisawa, H. Matsui, J. Takeya, *Nat. Commun.* **2016**, *7*, 11156.
[37] H. H. Choi, H. T. Yi, J. Tsurumi, J. J. Kim, A. L. Briseno, S. Watanabe, J. Takeya, K. Cho, V. Podzorov, *Adv. Sci.* **2020**, *7*, 1901824.
[38] D. Tahk, H. H. Lee, D.-Y. Khang, *Macromolecules* **2009**, *42*, 7079.
[39] M. A. Reyes-Martinez, A. Ramasubramaniam, A. L. Briseno, A. J. Crosby, *Adv. Mater.* **2012**, *24*, 5548.
[40] B. Geng, F. Zhang, C. Huang, L. He, C. Li, S. Duan, X. Ren, W. Hu, *J. Mater. Chem. C* **2024**, *12*, 5012.
[41] S. P. Timoshenko, J. N. Goodier, *Theory of Elasticity*, McGRAW-HILL, New York **1970**.
[42] M. T. Ruggiero, S. Ciuchi, S. Fratini, G. D'avino, *J. Phys. Chem. C* **2019**, *123*, 15897.
[43] M. Marinkovic, D. Belaineh, V. Wagner, D. Knipp, *Adv. Mater.* **2012**, *24*, 4005.
[44] H. Klauk, *Adv. Electron. Mater.* **2018**, *4*, 1700474.
[45] K. Kim, Y. Kim, *IEEE Trans. Electron Devices* **2010**, *57*, 2344.
[46] T. Zaki, S. Scheinert, I. Hörselmann, R. Rödel, F. Letzkus, H. Richter, U. Zschieschang, H. Klauk, J. N. Burghartz, *IEEE Trans. Electron Devices* **2013**, *61*, 98.
[47] T. Sawada, A. Yamamura, M. Sasaki, K. Takahira, T. Okamoto, S. Watanabe, J. Takeya, *Nat. Commun.* **2020**, *11*, 4839.
[48] T. Makita, S. Kumagai, A. Kumamoto, M. Mitani, J. Tsurumi, R. Hakamatani, M. Sasaki, T. Okamoto, Y. Ikuhara, S. Watanabe, J. Tkeya, *Proc. Natl. Acad. Sci. USA* **2020**, *117*, 80.